PAPER • OPEN ACCESS

Quantum-path signatures in attosecond helical beams driven by optical vortices

To cite this article: C Hernández-García et al 2015 New J. Phys. **17** 093029

View the article online for updates and enhancements.

Related content

- Macroscopic aspects of attosecond pulse generation
  Mette B Gaarde, Jennifer L Tate and Kenneth J Schafer

- Tailoring isolated attosecond pulses using quantum path interferences
  Carlos Hernández-García and Luis Plaja

- Spectral splitting and quantum path study of high-harmonic generation from a semi-infinite gas cell
  W Cao, G Laurent, Cheng Jin et al.

Recent citations

- High-order nonlinear dipole response characterized by extreme ultraviolet ellipsometry
  Kuang-Yu Chang et al

- Transverse phase matching of high-order harmonic generation in single-layer graphene
  Roberto Boyero-García et al

- Phase-matching analysis in high-order harmonic generation with nonzero orbital angular momentum Laguerre-Gaussian beams
  Cheng Jin et al

New Journal of Physics

The open access journal at the forefront of physics

CrossMark

PAPER

Quantum-path signatures in attosecond helical beams driven by optical vortices

C Hernández-García[1,2], J San Román[1], L Plaja[1] and A Picón[3]

[1] Grupo de Investigación en Óptica Extrema, Universidad de Salamanca, E-37008, Salamanca, Spain
[2] JILA, University of Colorado at Boulder, Boulder, CO 80309-0440, USA
[3] Argonne National Laboratory, Argonne, IL 60439, USA

E-mail: carloshergar@usal.es

Abstract

High-order harmonic generation (HHG) driven by beams carrying orbital angular momentum has been recently demonstrated as a unique process to generate spatio-temporal coherent extreme ultraviolet (XUV)/x-ray radiation with attosecond helical structure. We explore the details of the mapping of the driving vortex to its harmonic spectrum. In particular we show that the geometry of the harmonic vortices is complex, arising from the superposition of the contribution from the short and long quantum paths responsible of HHG. Transversal phase-matching and quantum path interferences provide an explanation of the dramatic changes in the XUV vortex structure generated at different relative positions of the target respect to the laser beam focus. Finally, we show how to take advantage of transversal phase-matching to select helical attosecond beams generated from short or long quantum paths, exhibiting positive or negative temporal chirp respectively.

Photons are traditionally assumed to carry one unit of angular momentum, the spin angular momentum, related to polarization. However it is now clear that photons can possess extra angular momentum, the orbital angular momentum (OAM), related to their transversal spatial profile [1–3]. Helical phased beams, also called optical vortices, with a transversal spiral-phase structure around the beam axis have a well-defined OAM. These singular beams have been commonly generated in the optical/IR regime and used in a wide range of applications, such as optical communication [4, 5], micromanipulation [6, 7], and phase-contrast microscopy [8, 9], among others [10]. However, there is a clear interest to bring helical phased beams into the extreme ultraviolet (XUV) and x-ray regime for microscopy and spectroscopy applications [11–15].

Schemes for the generation of helical phased beams in the XUV/x-ray regime have been reported at large facilities, such as synchrotrons and x-ray free-electron lasers [16–20]. It has been recently reported the generation of XUV vortices from table-top sources, via high-order harmonic generation (HHG) [21]. HHG is an extreme nonlinear process, customarily in an atomic gas-phase medium interacting with an intense laser beam, capable of producing coherent radiation at the XUV and soft x-ray spectral ranges [22]. The harmonic radiation presents unique characteristics, the higher orders being emitted in the form of pulse trains at the attosecond timescale [23, 24]. Harmonics with well-defined OAM (OAM–HHG) can be generated using helical phase beams as driving fields. The first experiment of OAM–HHG [21] reported harmonic vortices with topological charge nearly equal to that of the fundamental field. This is counterintuitive in terms of the understanding of HHG, in which the phase of the harmonics scales roughly with the harmonic order [25]. In fact, those experimental observations were attributed by the authors to nonlinear propagation effects and not to the OAM–HHG generation process itself. We have recently predicted that in HHG where nonlinear propagation effects are negligible, each harmonic is generated with a topological charge of $q\ell$ (q being the harmonic order and ℓ the topological charge of the driving field) [26]. Shortly afterwards, this was experimentally proven by Gariepy *et al* [15].

HHG spectra result from the interplay between the microscopic single-atom emission and the macroscopic superposition of the contributions of all the atoms in the medium. The single-atom emission is well described by
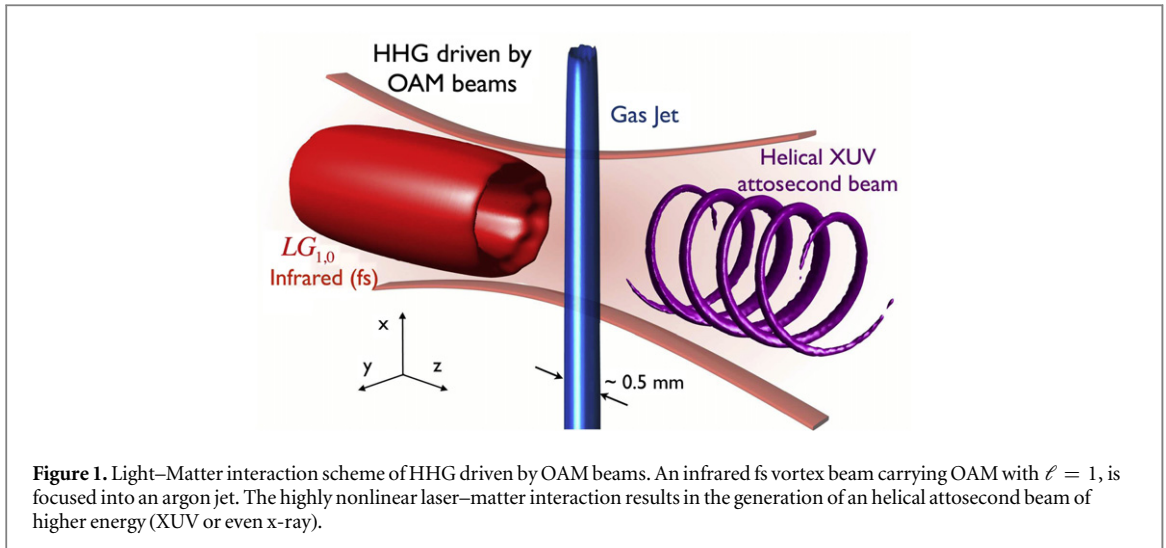
Figure 1. Light–Matter interaction scheme of HHG driven by OAM beams. An infrared fs vortex beam carrying OAM with $\ell = 1$, is focused into an argon jet. The highly nonlinear laser–matter interaction results in the generation of an helical attosecond beam of higher energy (XUV or even x-ray).

the so-called three-step model [27, 28]: an electron is tunnel-ionized by an intense laser; once in the continuum, it is accelerated by the field and driven back to the parent ion; finally, upon recollision, it can recombine emitting a high-frequency photon. The dynamics of the electron in the continuum can be described using classical trajectories, from which it is simple to associate a particular recombination energy with an initial (ionization) time. Interestingly enough, every half cycle there are two different electron paths leading to the same recombination energy, the so-called short and long trajectories. Short and long path contributions also emerge from the quantum framework, within strong-field approximation (SFA) [29, 30]. The phase of the harmonic emission depends on the particular path followed by the electron. The structure of the harmonic spectrum may be intricate, resulting from the interference of the emissions of the different paths. In addition, the time ordering of the short (long) paths gives rise to a positive (negative) chirp in the temporal structure of the associated attosecond pulses [31]. Finally, longer quantum paths, evolving over more than a laser cycle, give rise to higher-order rescatterings [32, 33], introducing zeptosecond modulations in the harmonic radiation driven by mid-infrared pulses [34]. Interferences in the HHG from short and long paths have been experimentally observed in standard HHG experiments [35]. However, the contributions of the different quantum paths on OAM–HHG have not been explored so far.

Macroscopically, the detected harmonic signal results from the coherent superposition of the emitted light from each atom in the gas-phase medium. Phase-matching is essential to understand most of the macroscopic features of HHG radiation, and to develop unique sources such as soft x-ray harmonics driven by mid-infrared lasers [22]. Phase-matching has been extensively studied for Gaussian beams focused into gas jets or gas cells [36–38] or transversal Bessel beams propagating in waveguides [39]. However, phase-matching of high-order harmonics driven by helical phase profiles carrying OAM remains completely unexplored.

In this work we perform the analysis of quantum path and phase-matching in OAM–HHG. By resorting to a simple model combining quantum-path concepts from SFA theory with classical diffraction, we explore the role of different quantum-path contributions on the phase-matching of HHG vortices. In particular, we unravel the dramatic changes in the structure of the harmonic vortices when changing the target position with respect to the focus of the laser beam. Finally, we show how to take advantage of transversal phase-matching to select helical attosecond beams generated from short or long quantum paths, and thus, exhibiting positive or negative temporal chirp.

1. Quantum-path OAM model

The physical scenario under study is sketched in figure 1. A pulsed vortex beam centered at 800 nm, a typical wavelength used for HHG, is focused into an argon gas jet. The laser pulse is assumed to have a temporal envelope $\sin^2(\pi t/NT)$, where $N = 16$ cycles and T is the period (2.67 fs). The FWHM of the pulse is 15.4 fs. The amplitude of the field E_0 is chosen to give a peak intensity of 1.4×10^{14} W cm^{-2} at the focus. The spatial structure of the vortex beam is represented by a monochromatic Laguerre–Gaussian beam propagating in the z-direction, with wavelength λ_0 ($k_0 = 2\pi/\lambda_0$), expressed as $LG_{\ell,p}(r, \phi, z; k_0)\mathrm{e}^{\mathrm{i}k_0 z}$ where

$$LG_{\ell,p}\left(r,\phi,z;k_0\right) = E_0 \frac{w_0}{w(z)}\left(\frac{\sqrt{2}r}{w(z)}\right)^{|\ell|} \times L_p^{|\ell|}\left(\frac{2r^2}{w^2(z)}\right)\exp\left(-\frac{r^2}{w^2(z)}\right)$$
$$\times \exp\left[i\ell\phi + i\frac{k_0 r^2}{2R(z)} + i\Phi_G(z)\right], \tag{1}$$

where $w(z) = w_0\sqrt{1+(z/z_0)^2}$ with w_0 being the waist of the mode, $z_0 = k_0 w_0^2/2$ the Rayleigh range, $R(z) = z[1+(z_0/z)^2]$ the phase-front radius, $\Phi_G(z) = -(2p+|\ell|+1)\arctan(z/z_0)$ the Gouy phase, and $L_p^{|\ell|}(x)$ the associated Laguerre polynomials

$$L_p^{|\ell|}(x) = \sum_{m=0}^{p}(-1)^m \frac{(|\ell|+p)!}{(p-m)!(|\ell|+m)!\,m!}x^m. \tag{2}$$

The indices $\ell = 0, \pm 1, \pm 2, \ldots$ and $p = 0, 1, 2, \ldots$ correspond to the topological charge and the number of nonaxial radial nodes of the mode, respectively.

We consider a laser pulse with a well-defined OAM of $\ell = 1$. The beam waist is $w_0 = 30\,\mu$m and, therefore, the Rayleigh range is $z_0 = 3.5$ mm. The detector is assumed to be far enough from the interaction area in order to comply with the far-field condition. In this work, we shall consider two targets: (i) a gas medium consisting of a thin layer (1 μm thick) placed perpendicularly to the pulse propagation axis, with homogeneous density of 10^{17} atoms cm^{-3}; (ii) a more realistic three-dimensional gas jet directed along the x-axis, and modeled by a Gaussian distribution along the y and z dimensions (whose FWHM is 500 μm), and a constant profile along its axial dimension, x, with a peak density of 10^{17} atoms cm^{-3}.

We have developed a simple model to gain insight on the physical origin of the structure of the XUV vortices generated via HHG. Our quantum-path OAM model assumes that all the radiation has been emitted from an infinitely thin gas layer, placed perpendicularly to the propagation axis of the fundamental beam. This approximation neglects the longitudinal phase-matching effects and allows us to focus the discussion on the transversal phase-matching [40], that becomes relevant due to the unique transversal structure of beams carrying OAM. The complex beam profile of the fundamental field in the thin layer, at a propagation position z_t, can be written as

$$A(\mathbf{r}) = U\left(r,z_t\right)e^{i\Phi\left(r,\phi,z_t\right)}, \tag{3}$$

where $\Phi(r,\phi,z_t)$ contains the phase terms in the exponential of equation (1), whereas the amplitude terms are grouped in $U(r,z_t)$.

We consider, therefore, the thin layer as a planar source of high-order harmonics, whose intensity profiles at the layer are related to that of the fundamental field. In the perturbative regime the amplitude of the generated radiation is proportional to the power of the fundamental beam amplitude, $\propto A^q$, where q is the order of the emitted harmonic. However, since HHG is highly non-perturbative, the amplitude of the generated field scales with a lower power A^p [25], where p is approximately constant for the harmonics with similar intensity, those located at the spectral plateau. In our case we use $p = 3.4$, which was obtained by calculating the HHG spectrum in the SFA+ [41] at different intensities. Then, the amplitude of the qth-order harmonic, $U_q(r,z_t)$, can be written as the superposition of the contributions from the long (L) and short (S) quantum paths

$$U_q^{(S)}\left(r,z_t\right) = \left(\frac{C}{\tau^{(S)}}\right)^{3/2}U^p\left(r,z_t\right), \tag{4}$$

$$U_q^{(L)}\left(r,z_t\right) = \left(\frac{C}{\tau^{(L)}}\right)^{3/2}U^p\left(r,z_t\right) \tag{5}$$

being C a constant and τ the time related to the quantum path [42], affecting the efficiency of HHG due to the quantum diffusion of the electronic wavepacket.

On the other hand, the phase of the harmonics is composed of the phase of the driving field times the harmonic order (q), and of the *intrinsic* phase of the HHG process, which is proportional to the intensity of the fundamental field [29, 35, 38, 43]. Therefore, the harmonic field at the target can be written as the superposition of the two contributions:

$$A_q^{(S)}(\mathbf{r}) = U_q^{(S)}\left(r,z_t\right)e^{iq\Phi\left(r,\phi,z_t\right)}e^{i\alpha_q^{(S)}I\left(r,z_t\right)}, \tag{6}$$

$$A_q^{(L)}(\mathbf{r}) = U_q^{(L)}\left(r,z_t\right)e^{iq\Phi\left(r,\phi,z_t\right)}e^{i\alpha_q^{(L)}I\left(r,z_t\right)}. \tag{7}$$

Once we have the description of the qth-harmonic field at the layer, we use Fraunhofer diffraction theory to calculate the far field at the detector. For a detector located at the position $(0, y, z)$, the qth-harmonic field along the y-axis is given by

$$A_q(\beta; z) = -\mathrm{i}\frac{\mathrm{e}^{\mathrm{i}k_q(z-z_\mathrm{t})(1+\beta^2/2)}}{\lambda_q(z-z_\mathrm{t})}\int_0^\infty\int_0^{2\pi} A_q\big(r', \theta'; z_\mathrm{t}\big)\mathrm{e}^{-\mathrm{i}\frac{2\pi}{\lambda_q}\beta r'\sin\theta'}r'\mathrm{d}r'\mathrm{d}\theta', \tag{8}$$

where β is a very small angle given by $\beta \approx y/z$ and (r', θ') represent the polar coordinates in the thin layer. λ_q is the wavelength of the qth-harmonic related to the fundamental wavelength as $\lambda_q = \lambda_0/q$, and then $k_q = 2\pi/\lambda_q = qk_0$. Now, using (6) or (7), we obtain

$$A_q^{(j)}(\beta; z) \propto \left(\frac{C}{\tau^{(j)}}\right)^{3/2}\int_0^\infty\int_0^{2\pi}r'\mathrm{d}r'\mathrm{d}\theta' U^p\big(r', z_\mathrm{t}\big)$$
$$\times\ \mathrm{e}^{\mathrm{i}q\Phi(r',\theta',z_\mathrm{t})}\mathrm{e}^{\mathrm{i}\alpha_q^{(j)}I}\mathrm{e}^{-\mathrm{i}\frac{2\pi}{\lambda_q}\beta r'\sin\theta'}, \tag{9}$$

where j can be S or L to represent the short and long trajectory contribution, respectively. By considering the phase part of the fundamental Laguerre–Gaussian beam, equation (1), and performing the integral over the angular coordinate, we finally obtain a compact formula that includes the dependence both on the fundamental OAM (ℓ) and on the quantum path contribution (j),

$$A_q^{(j)}(\beta; z) \propto \left(\frac{C}{\tau^{(j)}}\right)^{3/2}\int r'\mathrm{d}r' U^p\big(r', z_\mathrm{t}\big)$$
$$\times\ \mathrm{e}^{\mathrm{i}q\frac{k_0rr'^2}{2R(z_\mathrm{t})}}\mathrm{e}^{\mathrm{i}q\Phi_G(z_\mathrm{t})}\mathrm{e}^{\mathrm{i}\alpha_q^{(j)}I}J_{q\ell}\left(\frac{2\pi}{\lambda_q}\beta\ r'\right). \tag{10}$$

We should comment that the strong-field parameters $\alpha_q^{(j)}$ are found from the action of classical trajectories with recollision energies leading to the considered harmonic [38], for the 19th-order harmonic $\alpha_{19}^S = 2.76 \times 10^{-14}\ \mathrm{cm}^2\ \mathrm{W}^{-1}$ and $\alpha_{19}^L = 2.22 \times 10^{-13}\ \mathrm{cm}^2\ \mathrm{W}^{-1}$.

2. Quantum path contributions to OAM HHG

Harmonic phase-matching conditions are known to depend strongly on the position of the target with respect to the focus of the driving field [38]. In particular, in standard HHG experiments with Gaussian beams, short quantum paths remain as the only contributions to HHG if the gas target is placed after the focus position. On the other hand, if the target is placed before the focus, short quantum paths dominate for low divergence angles, while long ones dominate at larger angles [36, 37]. In this section we analyze the effect of the target position in HHG by helical-phase beams carrying OAM.

We start analyzing the HHG spectrum by using a 3D quantum model [44], including harmonic propagation. Our model calculates the coherent emission of every radiator in the gas medium and sum them coherently at the detector. The coherent emission of every atom is calculated in the quantum framework of the SFA+ approximation, an extension of the standard strong field approach with good quantitative accuracy [41]. Propagation effects of the fundamental field, including plasma and neutral dispersion as well as time-dependent group velocity walk-off [45], are all taken into account. The absorption of the harmonics in the gas is modeled using Beer's law. The method has been successfully used for describing regular HHG with near- and mid-IR lasers, in good agreement with experiments where macroscopic phase-matching plays a relevant role [22, 40, 46]. This method is ideal to compute high-order harmonic propagation in non-symmetric geometries, and therefore it is specially suited for computing HHG driven by beams carrying OAM [26].

Figure 2(a) shows the angular (β) dependence of the 19th harmonic yield, calculated by the 3D quantum model. Here, we consider the gas medium to be a thin layer of 1 μ m placed at different positions with respect to the focus of the beam, (i.e. different z_t), where $z_\mathrm{t} < 0$ ($z_\mathrm{t} > 0$) stands for a layer placed before (after) the focus position. For this type of target, with thickness smaller than the coherent length, the longitudinal phase-matching contributions are irrelevant. We observe that the divergence of the main emission significantly changes with respect to the layer position. Moreover, at large angles we also observe a weaker wriggle structure along the angular direction that dominates when the layer is after the focus position (at $z_t > 0$). Note that the horizontal axis can be interpreted as the radial axis of the emitted OAM ring.

In figures 2(b)–(d) we use our quantum-path OAM model in order to get a qualitatively explanation of the the features observed in figure 2(a). We integrate equation (10) with the same beam parameters used in figure 2(a) and we obtain figures 2(b) and (c) for short and long quantum path contributions, respectively, whereas in figure 2(d) we show the coherent addition of both contributions. Note that, in the later plot, we obtain an emission pattern that is very similar to the one calculated by the 3D quantum model in figure 2(a). This demonstrates that the quantum-path OAM model gives a qualitatively good description of the HHG process. Therefore, we can use figures 2(b) and (c) to track back the main features of figures 2(a) and relate them to the different quantum paths.
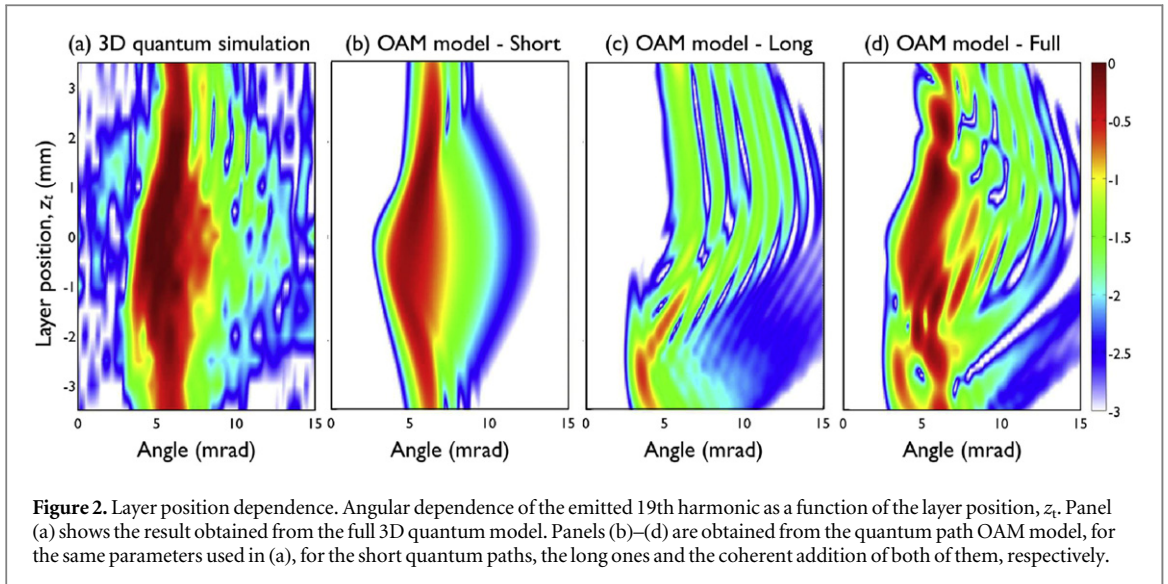
Figure 2. Layer position dependence. Angular dependence of the emitted 19th harmonic as a function of the layer position, z_t. Panel (a) shows the result obtained from the full 3D quantum model. Panels (b)–(d) are obtained from the quantum path OAM model, for the same parameters used in (a), for the short quantum paths, the long ones and the coherent addition of both of them, respectively.

We note that the emission dependence on the layer position is completely different for short and long quantum paths, and the overall emission is dominated by the short quantum path contribution. We can identify two different regimes, depending on the layer position respect to the focus. First, when the layer is placed before the focus ($z_t < 0$, long quantum paths are emitted with smaller divergence angle than the short ones. In fact, starting around $z_t = -2$ mm, in both figures 2(a) and (d) we can identify two well separated contributions, with similar weight, from long quantum paths at smaller angles and from short at higher angles. Second, when the layer is placed after the focus ($z_t > 0$), the short quantum path contributions dominate at smaller divergence angles, while the long ones generate a wriggle structure at large divergence angles.

In order to confirm that the qualitative picture given by the quantum-path OAM model is correct, and it is actually meaning the separation of short and long quantum paths in the angular dependence as we have discussed above, we perform a time–frequency analysis (TFA) based on the 3D quantum simulations. The 3D quantum model gives a full quantum description of the emitted radiation in HHG, but it does not provide an insight of the semiclassical picture of quantum trajectories. TFA can resolve the temporal order in which harmonics are being emitted. Short (long) quantum paths give rise to a positive (negative) chirp in the harmonic emission [31], and as a consequence, short (long) quantum paths will present a structure in the TFA with positive (negative) slope.

In figures 3(a) and (b) we show the TFA for two positions of the gas layer, 2 mm before and after the focus respectively, accordingly to the two regimes identified in figure 2. By looking at the harmonics located in the plateau region of the spectrum, between $q = 17$ and $q = 23$, the angle of the emitted radiation is smaller before focus ($z_t = -2$ mm) than after focus ($z_t = 2$ mm), in agreement with figure 2. For the case of the layer located before focus, we perform the TFA at 3.5 mrad (a1), and 6.2 mrad (a2). The TFA structures with negative and positive slope identify the contributions of long and short trajectories, respectively. Note that within each half-cycle, the long quantum path structures in (a1) are delayed in time with respect to the short ones in (a2), as expected from the semiclassical HHG theory [47].

Figure 3(b) shows the TFA for a target placed 2 mm after the focus, at three divergence angles 6.2 mrad (b1), 7.9 mrad (b2), and 8.8 mrad (b3). These angles are depicted in the left panel of figure 3(b), and correspond to three separated harmonic rings. We note that, in accordance with the quantum-path OAM model results of figure 2, (b1) is dominated by short quantum path contributions, whereas (b3) by long ones. Interestingly, the annular structure conformed around 7.9 mrad (b2) presents contributions from both short and long quantum paths, in agreement to the observation of figures 2(b)–(d).

3. Results for a 3D target

In the previous section we have shown that the main features of the angular HHG emission profile can be understood in terms of a simple quantum-path OAM model. However, the model and previous computations only account for transversal phase-matching by considering a thin gas layer. In a realistic HHG experiment the gas jet is a 3D object, and longitudinal phase-matching must be taken into account. To evaluate this later effect, we consider a 3D argon gas jet, with a thickness of 500 μm FWHM along the longitudinal direction (see section 1
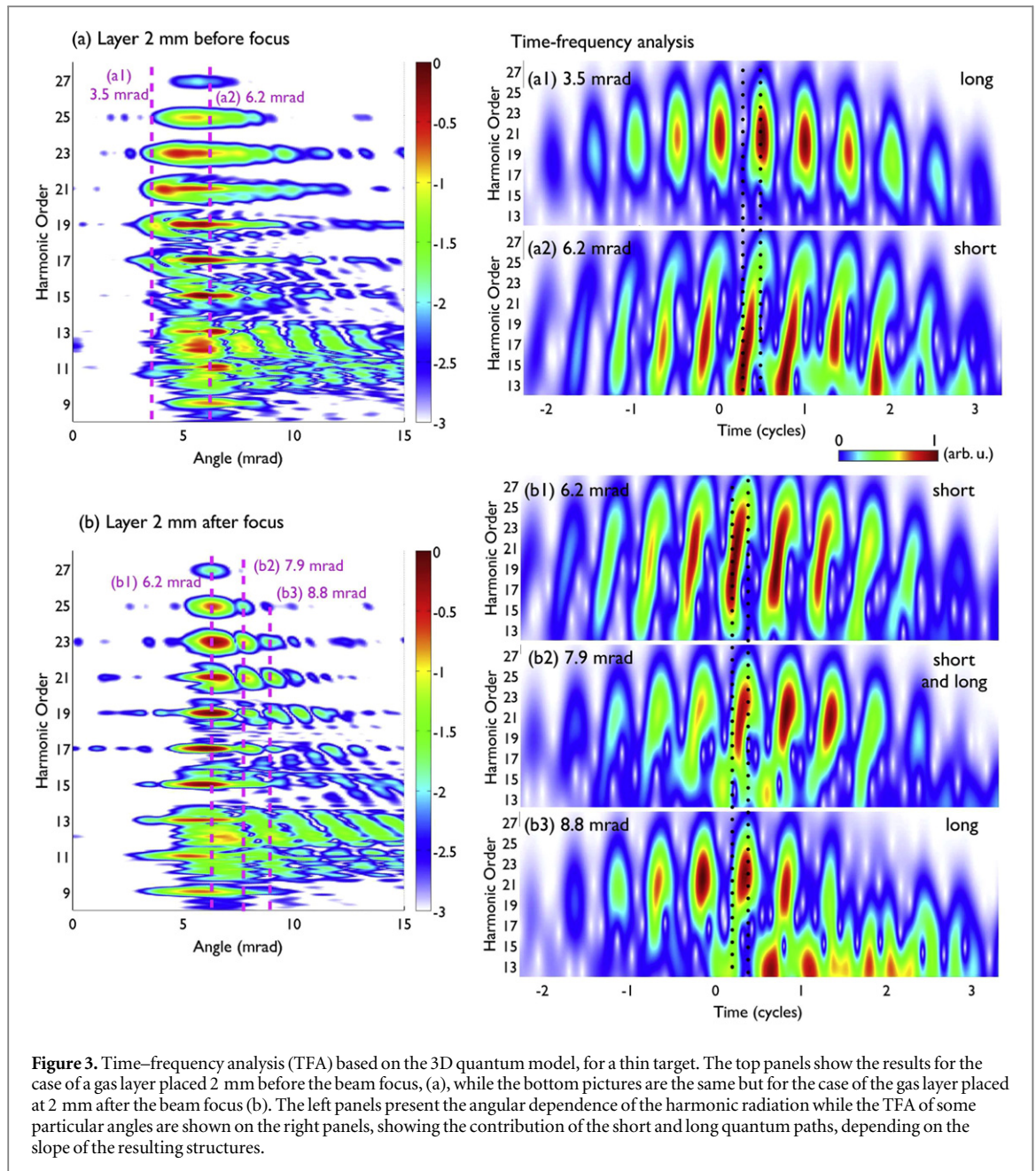
Figure 3. Time–frequency analysis (TFA) based on the 3D quantum model, for a thin target. The top panels show the results for the case of a gas layer placed 2 mm before the beam focus, (a), while the bottom pictures are the same but for the case of the gas layer placed at 2 mm after the beam focus (b). The left panels present the angular dependence of the harmonic radiation while the TFA of some particular angles are shown on the right panels, showing the contribution of the short and long quantum paths, depending on the slope of the resulting structures.

for more details about the jet profile), and we use our 3D quantum model to calculate the macroscopic far-field HHG signal.

In figure 4 we show the transversal structure of the 19th harmonic at the detector when the gas jet is placed 2 mm before (a) and after (b) the focus position. We present both the angular profiles of the intensity and the phase of the harmonic radiation. The intensity distribution of both cases shows the characteristic annular structure of a beam carrying OAM. In the phase distribution we observe that the high-order topological charge of the 19th harmonic is $\ell = 19$, as expected from the conservation of OAM in HHG [15, 26].

When the gas jet is placed before the focus (a), two different rings are observed, whose TFA analysis is shown in panels (a1) and (a2). In agreement with the predictions from the quantum-path OAM model, the inner ring (a1) results from long quantum paths, whereas the outer one (a2) from the short ones. Note that the angular divergence of the rings is well reproduced in our thin target calculations of the previous sections. While the topological charge is not affected by the quantum path taken by the electronic wave packet, the relative phase of the vortex rings reflect the fact that the different path contributions are delayed in time. On the other hand, when the gas jet is located after the focus (b), a prominent ring, and two secondary ones are observed. The TFA analysis also corroborate the results obtained from the quantum-path OAM model, showing that the more intense inner ring (b1) comes from short quantum paths, whereas the outer ring (b3) from the long ones. Again, the intermediate ring (b2) presents contributions from both short and long quantum paths. As a result, we conclude
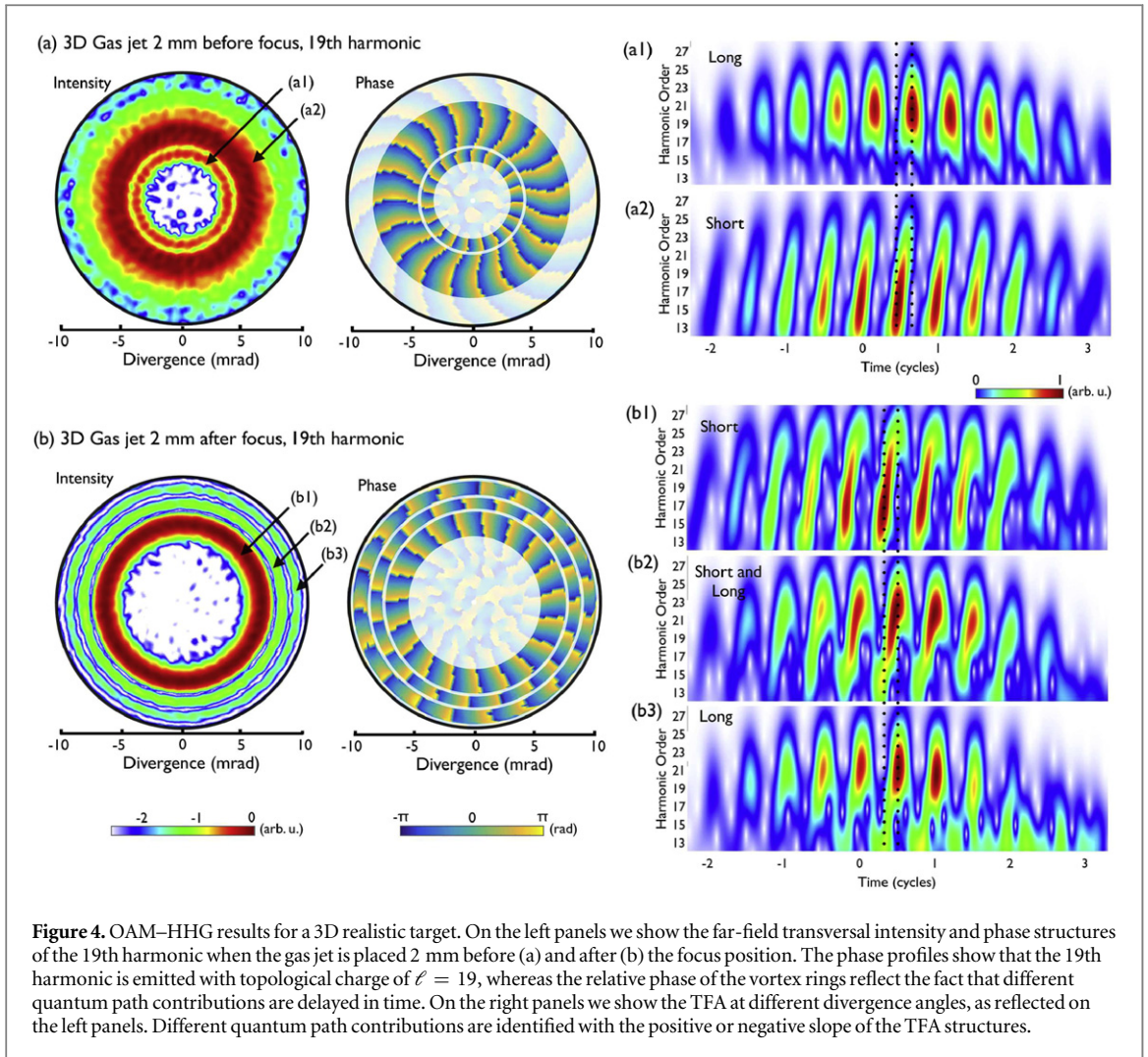
Figure 4. OAM–HHG results for a 3D realistic target. On the left panels we show the far-field transversal intensity and phase structures of the 19th harmonic when the gas jet is placed 2 mm before (a) and after (b) the focus position. The phase profiles show that the 19th harmonic is emitted with topological charge of $\ell = 19$, whereas the relative phase of the vortex rings reflect the fact that different quantum path contributions are delayed in time. On the right panels we show the TFA at different divergence angles, as reflected on the left panels. Different quantum path contributions are identified with the positive or negative slope of the TFA structures.

that longitudinal phase-matching does not modify our previous conclusions, and thus the angular separation of highly charged HHG vortices from different quantum paths is due to the transversal phase-matching. In addition, this corroborates the adequacy of the quantum-path OAM model developed in section 1.

4. Helical attosecond pulse trains and quantum path selection

We finally present in figure 5 the temporal structure of the two HHG spectra analyzed in figure 4, that correspond to the 3D argon gas jet case. In analogy to what was shown in [26], both cases present a helical attosecond pulse train structure, i.e., an attosecond pulse train delayed along the azimuthal coordinate according to the phase variation of the fundamental OAM beam. Note that the helical beam structure is a result of the addition of harmonic vortices with different topological charges [48]. We can observe different helical pulse trains (which for convenience they are plotted in different colors) associated to the path contributions described in the previous section. In addition, four transversal snapshots are shown at different time steps within a half-cycle. When the gas jet is placed before the focus (figure 5(a)), two helical attosecond pulse trains are emitted: the inner one (a1, green) generated by long quantum paths, and the outer one (a2, pink), by short quantum paths. With the help of the attosecond pulse trains at azimuthal angle equal to zero plotted in (a1) and (a2), we observe that the long quantum path attosecond pulse train is delayed in time, as expected from the HHG theory. This can be also confirmed in the transversal snapshots, where the long (inner) and short (outer) contributions appear at different positions at the same time.

Analogous, when the gas jet is placed after the focus position (figure 5(b)) we can select three different helical attosecond pulse trains from short (a1, pink), short and long (a2, yellow) and long (a3, green) quantum paths. In the transversal snapshots and in the attosecond pulse trains at azimuthal angle equal to zero, we can observe how the helical structures are delayed in time accordingly to the nature of their quantum path contribution.
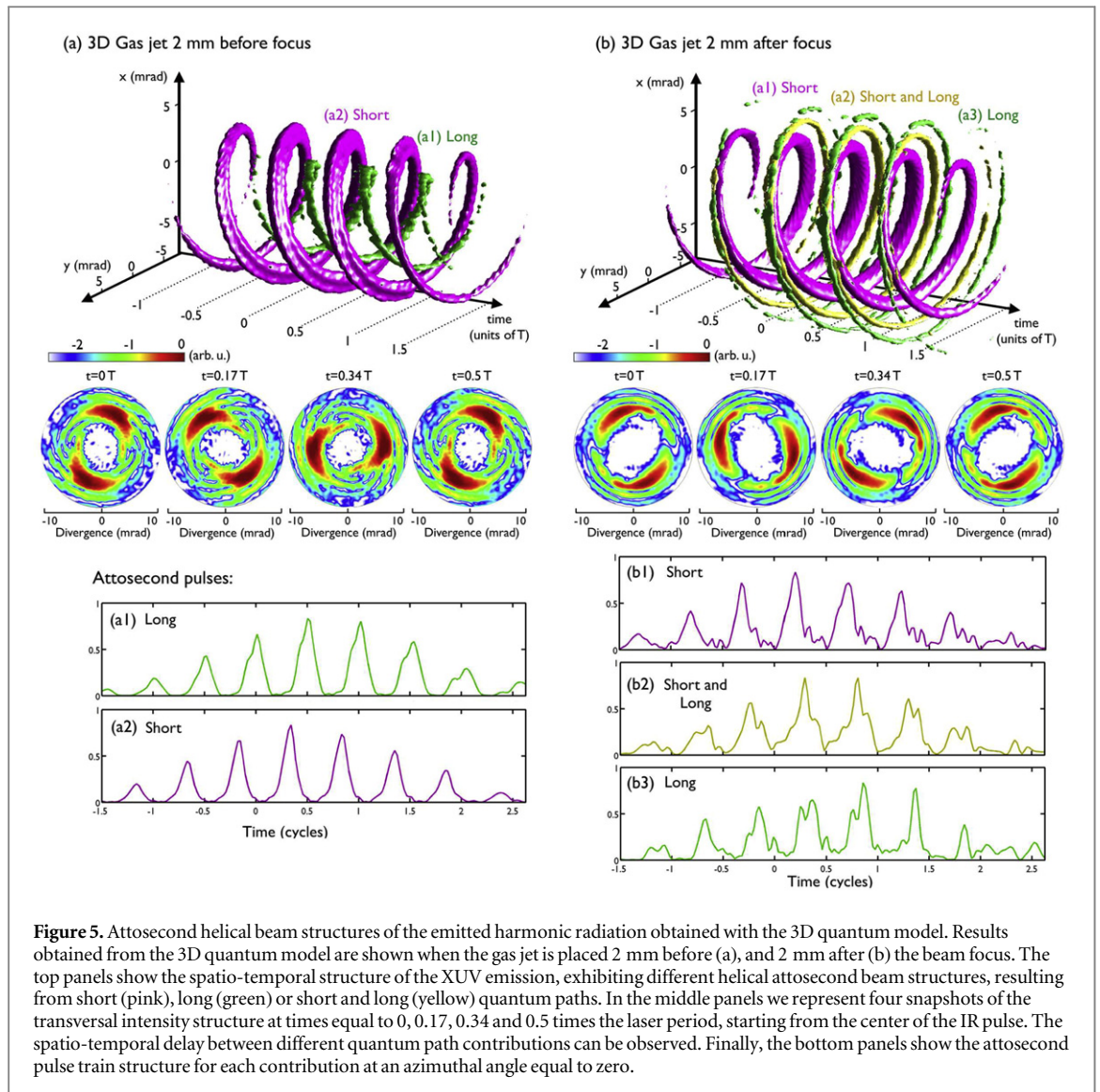
Figure 5. Attosecond helical beam structures of the emitted harmonic radiation obtained with the 3D quantum model. Results obtained from the 3D quantum model are shown when the gas jet is placed 2 mm before (a), and 2 mm after (b) the beam focus. The top panels show the spatio-temporal structure of the XUV emission, exhibiting different helical attosecond beam structures, resulting from short (pink), long (green) or short and long (yellow) quantum paths. In the middle panels we represent four snapshots of the transversal intensity structure at times equal to 0, 0.17, 0.34 and 0.5 times the laser period, starting from the center of the IR pulse. The spatio-temporal delay between different quantum path contributions can be observed. Finally, the bottom panels show the attosecond pulse train structure for each contribution at an azimuthal angle equal to zero.

These results confirm that short and long quantum path contributions can be spatio-temporally selected in the generation of highly charged XUV vortices by HHG. In addition, helical attosecond pulse trains are emitted, with different time delays, and different chirp, being positive for the short quantum path contributions and negative for the short ones. Thus, our results show the possibility of generating helical attosecond pulse trains with different spatio-temporal structures that could be selected depending on the application. These type of helical beams, where not only the phase but also the intensity profile have an helical structure, are beams able to exchange OAM in situations where standard Laguerre–Gauss beams cannot, opening an entire new light–matter interaction regime, [48].

Experimental methods to produce driving fields with well-defined OAM can be imperfect. Spiral-phase plates or spatial light modulators are design for a specific wavelength and ultrashort pulses may generate beams with fractional OAM [49] at wavelengths within the pulse bandwidth. The pulses studied here are long enough to neglect those imperfections. However, a further analysis of the phase-matching effects is needed in a more realistic scenario when few-cycle pulses are considered.

5. Conclusion

We have performed an analysis of the spatio-temporal structure of the XUV vortices generated by harmonic conversion of a driving field carrying a well-defined OAM. A simple model based on SFA quantum-path concepts combined with classical diffraction, reveals the fundamental role of transversal phase-matching in conforming the complex diverging structure of the macroscopic emission. The model allows to disentangle the contributions coming from the short and long quantum paths. We show that the harmonic emission can be

modified by the relative position between the jet gas and the beam focus, in a completely different way to HHG driven by Gaussian beams (no-OAM). If the gas jet is placed before focus, the radiation coming from long quantum paths is emitted at a smaller divergence than that from the short ones. However, if the get is placed after focus, short quantum path contributions are emitted at a smaller divergence angle than long ones. Finally, we have also shown that this divergence dependency is preserved for several harmonics in the plateau. By filtering out the high-order harmonics in the plateau, different helical attosecond beams are emitted resulting from contributions from short and long quantum paths, and thus, with different spatio-temporal structure. We support our model with comparisons with full quantum calculations in the most relevant situations, including more realistic gas-jet targets.

Acknowledgments

References

[1] Allen L, Beijersbergen M W, Spreeuw R J C and Woerdman J P 1992 *Phys. Rev.* A **45** 8185
[2] Soskin M S and Vasnetsov M V 2001 *Prog. Opt.* **42** 219–76
[3] Calvo G F, Picón A and Bagan E 2006 *Phys. Rev.* A **73** 013805
[4] Wang J *et al* 2012 *Nat. Photonics* **6** 488–96
[5] Cai X, Wang J, Strain M J, Johnson-Morris B, Zhu J, Sorel M, O'Brien J L, Thompson M G and Yu S 2012 *Science* **338** 363
[6] Simpson N, Allen L and Padgett M 1996 *J. Mod. Opt.* **43** 2485–91
[7] Grier D G 2003 *Nature* **424** 810
[8] Fürhapter S, Jesacher A, Bernet S and Ritsch-Marte M 2005 *Opt. Lett.* **30** 1953
[9] Jesacher A, Fürhapter S, Bernet S and Ritsch-Marte M 2005 *Phys. Rev. Lett.* **94** 233902
[10] Torres J P and Torner L (ed) 2011 *Twisted Photons* (Weinheim: Wiley)
[11] Sakdinawat A and Liu Y 2007 *Opt. Lett.* **32** 2635
[12] van Veenendaal M and McNulty I 2007 *Phys. Rev. Lett.* **98** 157401
[13] Nugent K A 2010 *Adv. Phys.* **59** 1
[14] Picón A, Benseny A, Mompart J, Vázquez de Aldana J R, Plaja L, Calvo G F and Roso L 2010 *New J. Phys.* **12** 083053
[15] Gariepy G, Leach J, Kim K T, Hammond T J, Frumker E, Boyd R W and Corkum P B 2014 *Phys. Rev. Lett.* **113** 153901
[16] Peele A G, McMahon P J, Paterson D, Tran C Q, Mancuso A P, Nugent K A, Hayes J P, Harvey E, Lai B and McNulty I 2002 *Opt. Lett.* **27** 1752
[17] Sasaki S and McNulty I 2008 *Phys. Rev. Lett.* **100** 124801
[18] Hemsing E, Marinelli A and Rosenzweig J B 2011 *Phys. Rev. Lett.* **106** 164803
[19] Ribič P R, Gauthier D and de Ninno G 2014 *Phys. Rev. Lett.* **112** 203602
[20] Hemsing E, Stupakov G, Xiang D and Zholents A 2014 *Rev. Mod. Phys.* **86** 897
[21] Zürch M, Kern C, Hansinger P, Dreischuh A and Spielmann C 2012 *Nat. Phys.* **8** 743–6
[22] Popmintchev T *et al* 2012 *Science* **336** 1287
[23] Paul P M, Toma E S, Breger P, Mullot G, Augé F, Balcou P, Muller H G and Agostini P 2001 *Science* **292** 1689
[24] Goulielmakis E *et al* 2008 *Science* **320** 1614
[25] L'Huillier A, Balcou P, Candel S, Schafer K J and Kulander K C 1992 *Phys. Rev.* A **46** 2778
[26] Hernández-García C, Picón A, San Román J and Plaja L 2013 *Phys. Rev. Lett.* **111** 083602
[27] Corkum P B 1993 *Phys. Rev. Lett.* **71** 1994
[28] Schafer K, Yang B, DiMauro L F and Kulander K C 1993 *Phys. Rev. Lett.* **70** 1599
[29] Lewenstein M, Salieres P and L'Huillier A 1995 *Phys. Rev.* A **52** 4747
[30] Bellini M, Lynga C, Tozzi A, Gaarde M, Hänsch T, L'Huillier A and Wahlström C 1998 *Phys. Rev. Lett.* **81** 297–300
[31] Mairesse Y *et al* 2003 *Science* **302** 1540
[32] Tate J, Auguste T, Muller H G, Salières P, Agostini P and di Mauro L F 2007 *Phys. Rev. Lett.* **98** 013901
[33] Hickstein D D *et al* 2012 *Phys. Rev. Lett.* **109** 073004
[34] Hernández-García C, Pérez-Hernández J A, Popmintchev T, Murnane M M, Kapteyn H C, Jaroń-Becker A, Becker A and Plaja L 2013 *Phys. Rev. Lett.* **111** 033002
[35] Zaïr A *et al* 2008 *Phys. Rev. Lett.* **100** 143902
[36] Salières P, L'Huillier A and Lewenstein M 1995 *Phys. Rev. Lett.* **74** 3776
[37] Balcou P, Salieres P, L'Huillier A and Lewenstein M 1997 *Phys. Rev.* A **55** 3204
[38] Gaarde M B, Tate J L and Schafer K J 2008 *J. Phys. B: At. Mol. Opt. Phys.* **41** 132001
[39] Popmintchev T, Chen M-C, Bahabad A, Gerrity M, Sidorenko P, Cohen O, Christov I P, Murnane M M and Kapteyn H C 2009 *Proc. Natl Acad. Sci. USA* **106** 10516
[40] Hernández-García C, Sola I J and Plaja L 2013 *Phys. Rev.* A **88** 043848
[41] Pérez-Hernández J A, Roso L and Plaja L 2009 *Opt. Exp.* **17** 9891
[42] Lewenstein M, Balcou P, Yu M, Ivanov A, L'Huillier and Corkum P B 1994 *Phys. Rev.* A **49** 2117
[43] Hernández-García C and Plaja L 2012 *J. of Phys. B: At. Mol. Opt. Phys.* **45** 074021

[44] Hernández-García C, Pérez-Hernández J A, Ramos J, Conejero Jarque E, Roso L and Plaja L 2010 *Phys. Rev.* A **82** 022432
[45] Hernández-García C, Popmintchev T, Kapteyn H C, Murnane M M, Plaja L, Becker A and Jaron-Becker A 2015 submitted
[46] Hernández-García C, Holgado W, Plaja L, Alonso B, Silva F, Miranda M, Crespo H and Sola I J 2015 *Opt. Exp.* **16** 21497–508
[47] Antoine P, L'Huillier A and Lewenstein M 1996 *Phys. Rev. Lett.* **77** 1234–7
[48] Pariente G and Quéré F 2015 *Opt. Lett.* **40** 2037–40
[49] Leach J *et al* 2004 *New J. Phys.* **6** 71